Stability of Underwater Periodic Locomotion

Fangxu Jing and Eva Kanso

April 23, 2013

Abstract

Most aquatic vertebrates swim by lateral flapping of their bodies and caudal fins. While much effort has been devoted to understanding the flapping kinematics and its influence on the swimming efficiency, little is known about the stability (or lack of) of periodic swimming. In this paper, we examine the stability of periodic locomotion due to sideways flapping in unbounded potential flow. It is believed that stability limits maneuverability and body designs/flapping motions that are adapted for stable swimming are not suitable for high maneuverability and vice versa. Here, we consider a simplified model where the swimmer is a planar elliptic body undergoing prescribed periodic heaving and pitching. We show that periodic locomotion can be achieved due to the resulting hydrodynamic forces, and its value depends on several parameters including the aspect ratio of the body, the amplitudes and phases of the prescribed flapping. We obtain closed-form solutions for the locomotion and efficiency for small flapping amplitudes, and numerical results for finite flapping amplitudes. We then study the stability of the (finite amplitude flapping) periodic locomotion using Floquet theory. We find that stability depends nonlinearly on all parameters. Interesting trends of switching between stable and unstable motions emerge and evolve as we continuously vary the parameter values. This suggests that, when it comes to live organisms, maneuverability and stability need not be thought of as disjoint properties, rather the organism may manipulate its motion in favor of one or the other depending on the task at hand.

1 Introduction

A large proportion of fish species are characterized by elongated bodies that swim forward by flapping sideways. These sideways oscillations produce periodic propulsive forces that cause the fish to swim along time-periodic trajectories, [1]. The kinematics of the flapping motion and the resulting swimming performance, as well as their relationship to the swimmer's morphology, have been the subject of numerous studies, see, for example, [2, 3]. However, little attention has been given to the stability of underwater locomotion. The importance of motion stability and its mutual influence on body morphology and behavior is noted in the work of Weihs, see [4] and references therein. In [4], Weihs used clever arguments and simplifying approximations founded on a deep understanding of the equations governing underwater locomotion to obtain "educated estimates" of the stability of swimming fish without ever solving the complicated set of equations.

The main objective of this paper is to study the stability of periodic locomotion resulting from periodic sideways flapping. The locomotion is said to be unstable if a perturbation in the conditions surrounding the swimmer's body result in forces and moments that tend to increase the perturbation, and it is stable if these emerging forces tend to reduce such perturbations or keep them bounded so that the fish returns to or stays near its original periodic swimming.

Stability may be achieved actively or passively. Active stabilization requires neurological control that activate musculo-skeletal components to compensate for external perturbations acting against stability. On the other hand, passive stability of the locomotion gaits requires no additional energy input by the fish. In this sense, one can argue that stability reduces the energetic cost of locomotion. Therefore, from an evolutionary perspective, it seems reasonable to conjecture that stability would have a positive selection value in behaviors such as migration over prolonged distances and time. However, stability limits maneuverability, and body designs/flapping motions that are adapted for stable swimming are not suitable for high maneuverability and vice versa, [4, 5].

In this work, we study stability of periodic swimming using a simple model consisting of a planar elliptic body undergoing prescribed flapping motion in unbounded potential flow. By flapping motion, we mean periodic heaving and pitching of the body as shown in Figure 1. We formulate the equations of motion governing the resulting locomotion and examine its efficiency. We then investigate the stability of this motion using Floquet theory (see [6]). We find that stability depends in a non-trivial way on the body geometry (aspect ratio of the ellipse) as well as on the amplitudes and phases of the flapping motion. Most remarkable is the ability of the system to transition from stability to instability and back to stability as we vary some of these parameters.

This model is reminiscent of the three-link swimmer used by Kanso *et al.* to examine periodic locomotion in potential flow, see [7]. The three-link swimmer undergoes periodic shape deformations that result in coupled heaving, pitching and locomotion. Here, we ignore body deformations for the sake of simplicity and prescribe the heaving and pitching motion directly. Note that the three-link swimmer was also used by Jing & Kanso to study the effect of body elasticity on the stability of the coast motion of fish (motion at constant speed). They found that elasticity of the body may lead to passive stabilization of the (otherwise unstable) coast motion, see [8, 9]. The present model consisting of a single elliptic body is mostly similar to the system studied by Spagnolie *et al.* both experimentally and numerically, [10]. In the latter, an elliptic body undergoes passive pitching (via a torsional spring) subject to prescribed periodic heaving in viscous fluid, whereas in our model both the pitching and heaving motions are prescribed and the fluid medium is inviscid. Despite these differences, the two models exhibit qualitatively similar behavior as discussed in Section 6.

The paper is organized as follows. In Section 2, we formulate the equations of motion governing the locomotion of a periodically flapping body in unbounded potential flow. We analyze the body's locomotion and efficiency when subject to small amplitude flapping motion in Section 3, and consider the more general case of finite amplitude flapping in Section 4. In Section 5, we assess the stability of the periodic locomotion using Floquet theory. The main findings and their relevance are discussed in Section 6.

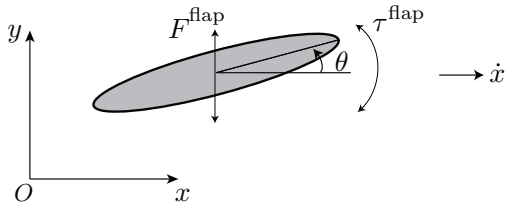

Figure 1: Model of flapping fish: An ellipse with semi-axes a and b is submerged in unbounded potential fluid. Motion is observed in inertial frame with position of mass center given by (x, y) and orientation by θ. Fish flaps in y- and θ-directions, and propels in x-direction.

2 Problem Formulation

Consider a planar elliptic body with semi-major axis a and semi-minor axis b, submerged in unbounded potential flow that is at rest at infinity. The elliptic body is neutrally buoyant, that is to say, the body and fluid densities are equal to ρ. The body's mass is given by $m_b = \rho\pi ab$, and its moment of inertia about the center of mass C is $J_b = m_b(a^2 + b^2)/4$. Let (x, y) denote the position of the mass center with respect to a fixed inertial frame and let θ denote the orientation angle of the ellipse measured from the positive x-direction to the ellipse's major axis, see Figure 1. The linear and angular velocities are given by $(\dot{x}, \dot{y})$ and $\dot{\theta}$, respectively, where the dot $\dot{()}$ correspond to derivative with respect to time t.

In order to emulate the flapping motion of a swimming body, we assume that y and θ vary periodically in time due to some periodic flapping force F^{flap} and flapping moment τ^{flap} generated by the swimming body. Note that in the case of a body swimming by deforming itself, y and θ are a result of the body deformation. Here, we do not account for the body deformation but rather prescribe $y(t)$ and $\theta(t)$ as periodic functions of time. Namely, we set

$$y(t) = A_y \sin(\omega t + \phi_y), \qquad \theta(t) = A_\theta \sin(\omega t + \phi_\theta). \tag{1}$$

and solve for the resulting locomotion in the x-direction.

The equations governing the motion of the flapping body are basically Kirchhoff's equations expressed in inertial frame and subject to forcing F^{flap} and τ^{flap} in the y- and θ-directions, that is,

$$m_b\,\ddot{x} = F_x, \tag{2}$$

and

$$m_b\,\ddot{y} = F_y + F^{\text{flap}}, \qquad J_b\,\ddot{\theta} = \tau + \tau^{\text{flap}}, \tag{3}$$

where F_x, F_y and τ are the hydrodynamic forces and moment acting on the body. For motions in potential flow, F_x, F_y and τ can be obtained using a classic procedure, see Appendix A,

$$\begin{aligned}
F_x &= \frac{1}{2}\left[-(m_1 + m_2) + (m_2 - m_1)\cos 2\theta\right]\ddot{x} + \frac{1}{2}(m_2 - m_1)\ddot{y}\sin 2\theta - (m_2 - m_1)(\dot{x}\sin 2\theta - \dot{y}\cos 2\theta)\dot{\theta},\\
F_y &= \frac{1}{2}\left[-(m_1 + m_2) - (m_2 - m_1)\cos 2\theta\right]\ddot{y} + \frac{1}{2}(m_2 - m_1)\ddot{x}\sin 2\theta + (m_2 - m_1)(\dot{x}\cos 2\theta + \dot{y}\sin 2\theta)\dot{\theta},\\
\tau &= -J\ddot{\theta} + \frac{1}{2}(m_2 - m_1)\left(\dot{x}^2\sin 2\theta - \dot{y}^2\sin 2\theta - 2\dot{x}\dot{y}\cos 2\theta\right).
\end{aligned} \tag{4}$$

Here $m_1 = \rho\pi b^2$, $m_2 = \rho\pi a^2$ are, respectively, the added mass of the elliptic body along its major and minor directions and $J = \rho\pi(a^2 - b^2)^2/8$ is the added moment of inertia [11]. Substituting (4) into (2) and (3), one can use (2) to solve for $x(t)$, and (3) to compute the forcing F^{flap} and τ^{flap} needed in order for the body to achieve the prescribed flapping motion in (1).

The total angular momentum h of the body-fluid system is given by $h = (J_b + J)\dot{\theta}$ whereas the total linear momentum can be written as the following

$$\begin{pmatrix} p_x \\ p_y \end{pmatrix} = m_b \begin{pmatrix} \dot{x} \\ \dot{y} \end{pmatrix} + \begin{pmatrix} \cos\theta & -\sin\theta \\ \sin\theta & \cos\theta \end{pmatrix} \begin{pmatrix} m_1 & 0 \\ 0 & m_2 \end{pmatrix} \begin{pmatrix} \cos\theta & \sin\theta \\ -\sin\theta & \cos\theta \end{pmatrix} \begin{pmatrix} \dot{x} \\ \dot{y} \end{pmatrix}. \tag{5}$$

The momentum p_x is conserved since there is no external forcing applied in the x direction. Therefore, one has $p_x(t) = p_x(t = 0)$, which yields

$$\dot{x}(t) = \frac{m_1 - m_2}{2\left(m_b + m_1\cos^2\theta + m_2\sin^2\theta\right)} \left[(\dot{y}\sin 2\theta)_{t=0} - (\dot{y}\sin 2\theta)\right]. \tag{6}$$

That is to say, equation (2) admits an integral of motion whose value is given by the above equation. The distance traveled by the body's center of mass in one period of flapping, $T = 2\pi/\omega$, is given by

$$d = \left|\int_0^T \dot{x}\,\mathrm{d}t\right| = |x(T) - x(0)|. \tag{7}$$

The total kinetic energy E of the body-fluid system is given by

$$E = \frac{1}{2}(\dot{x}\,p_x + \dot{y}\,p_y) + \frac{1}{2}(J_b + J)\dot{\theta}^2. \tag{8}$$

By the work-energy theorem, the time derivative of the kinetic energy is equal to the total power input by the flapping force F^{flap} and moment τ^{flap}. Thus, the work done by flapping is equivalent to the kinetic energy E. To this end, the average work done in one period is given by

$$\bar{E} = \frac{1}{T}\int_0^T E(t)\mathrm{d}t. \tag{9}$$

We define the *cost of locomotion* e as the average work divided by the average distance over one period, namely

$$e = \frac{\bar{E}}{d}. \tag{10}$$

Hence, smaller e means less energy expenditure for a fixed distance traveled. Therefore, it is convenient to denote the *efficiency* of the system η as the inverse of the cost of locomotion, that is $\eta \equiv 1/e = d/\bar{E}$.

Before we proceed to examining the locomotion and efficiency of such swimmer, it is convenient to non-dimensionalize the system by scaling time with T, length with $\sqrt{ab}$ and mass with $m_b = \rho\pi ab$. The variables are subsequently written in dimensionless form. The important parameters for this system are: aspect ratio $\gamma \equiv a/b$, amplitudes A_y and A_θ, and phases ϕ_y and ϕ_θ.

3 Small Flapping Amplitudes

Consider the case with small flapping amplitudes A_y and A_θ, that is to say, let $A_y \equiv \epsilon_y \ll 1$ and $A_\theta \equiv \epsilon_\theta \ll 1$ where both ϵ_y and ϵ_θ are of the same order of magnitude. Hence, one has $y, \dot{y}, \ddot{y} \sim O(\epsilon_y)$ and $\theta, \dot{\theta}, \ddot{\theta} \sim O(\epsilon_\theta)$, but ω, ϕ_y and ϕ_θ are not necessarily small. Take the approximation $\cos\theta \approx 1$ and $\sin\theta \approx \theta$ and substitute into (6) to obtain

$$\dot{x} \approx \frac{1}{2}(\gamma - 1)\,\omega\epsilon_y\epsilon_\theta\left[\sin(2\omega t + \phi_y + \phi_\theta) - \sin(\phi_y + \phi_\theta)\right]. \tag{11}$$

Clearly, the velocity in the x direction depends on the aspect ratio γ and $\phi_y + \phi_\theta$. This suggests that as long as $\phi_y + \phi_\theta = 2n\pi + \text{constant}$, $\dot{x}$ is the same function of time. Its magnitude is of order $\sim O(\epsilon_y\epsilon_\theta)$. In other words, for small amplitude flapping, the motion in x is small compared to the flapping motion in y and θ. Approximating expressions of F^{flap} and τ^{flap} are obtained by substituting (1) and (11) into (3), which yields

$$F^{\text{flap}} \approx (m_b + m_2)\ddot{y}, \qquad \tau^{\text{flap}} \approx (J_b + J)\ddot{\theta}. \tag{12}$$

For small amplitude flapping, we can express the cost of locomotion in closed form

$$e \approx \frac{\pi\left[\gamma(\gamma+1)\epsilon_y^2 + 2(\gamma^2+1)\epsilon_\theta^2\right]}{2\gamma(\gamma-1)\epsilon_y\epsilon_\theta|\sin(\phi_y + \phi_\theta)|}. \tag{13}$$

Hence, to minimize e (or, equivalently, to maximize efficiency η), one needs

$$\gamma \to \infty, \qquad \text{and} \qquad \phi_y + \phi_\theta = \left(n + \frac{1}{2}\right)\pi, \quad n = 0,\ \pm 1,\ \pm 2, \ldots \tag{14}$$

For large amplitudes A_y and A_θ, one does not have a closed form expression for e, hence the efficiency needs to be analyzed numerically, as done in the next section.

4 Locomotion and Efficiency

In this section, we examine the swimming trajectories and their dependence on the following parameters: aspect ratio γ, amplitudes A_y and A_θ, and phases ϕ_y and ϕ_θ. The swimming motion is given by (1) and (6), where the latter is integrated numerically to get $x(t)$.

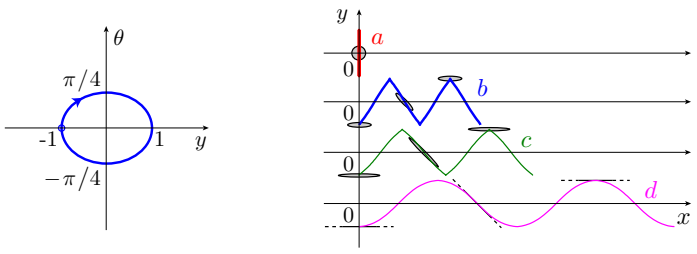

Figure 2: (color online) Left: Prescribed flapping in (y, θ) plane. Initial points are marked by $\circ$. Right: Trajectories of mass center in (x, y) plane with snapshots of body in motion overlaid. Simulations are for $A_y = 1, A_\theta = \frac{\pi}{4}, \phi_y = -\frac{\pi}{2}, \phi_\theta = 0$ and various aspect ratios: (a) $\gamma = 1.01$, (b) $\gamma = 4$, (c) $\gamma = 8$, (d) $\gamma = 1000$.

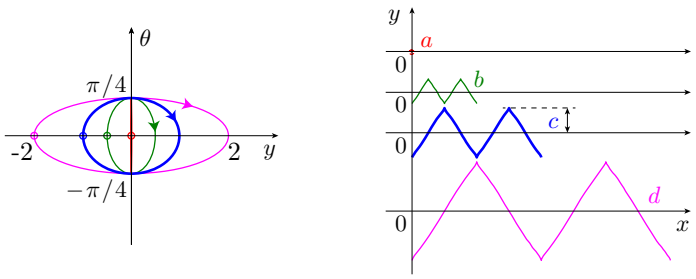

Figure 3: (color online) Left: Prescribed flapping in (y, θ) plane. Initial points are marked by $\circ$. Right: Trajectories of mass center in (x, y) plane. Simulations are for $A_\theta = \frac{\pi}{4}, \gamma = 4, \phi_y = -\frac{\pi}{2}, \phi_\theta = 0$ and various heaving amplitudes: (a) $A_y = 0.01$, (b) $A_y = 0.5$, (c) $A_y = 1$, (d) $A_y = 2$.

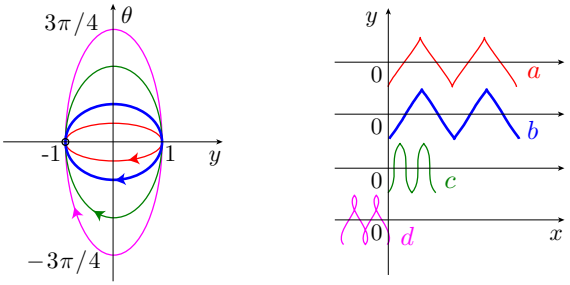

Figure 4: (color online) Left: Prescribed flapping in (y, θ) plane. Initial points are marked by $\circ$. Right: Trajectories of mass center in (x, y) plane. Simulations are for $A_y = 1, \gamma = 4, \phi_y = -\frac{\pi}{2}, \phi_\theta = 0$ and various pitching amplitudes: (a) $A_\theta = \pi/8$, (b) $A_\theta = \pi/4$, (c) $A_\theta = \pi/2$, (d) $A_\theta = 3\pi/4$.

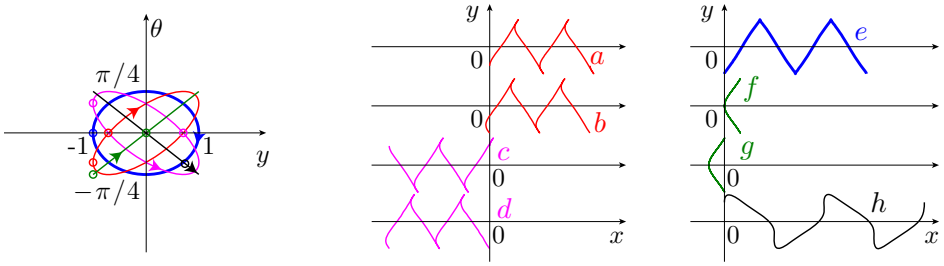

Figure 5: (color online) Left: Prescribed flapping in (y, θ) plane. Initial points are marked by $\circ$. Middle and right: Trajectories of mass center in (x, y) plane. Simulations are for $A_y = 1, A_\theta = \frac{\pi}{4}, \gamma = 4$ and various combinations of phases: (a) $(\phi_y, \phi_\theta) = (-\frac{\pi}{4}, 0)$, (b) $(\phi_y, \phi_\theta) = (-\frac{\pi}{2}, -\frac{\pi}{4})$, (c) $(\phi_y, \phi_\theta) = (\frac{\pi}{4}, 0)$, (d) $(\phi_y, \phi_\theta) = (-\frac{\pi}{2}, -\frac{3\pi}{4})$, (e) $(\phi_y, \phi_\theta) = (-\frac{\pi}{2}, 0)$, (f) $(\phi_y, \phi_\theta) = (0, 0)$, (g) $(\phi_y, \phi_\theta) = (-\frac{\pi}{2}, -\frac{\pi}{2})$, (h) $(\phi_y, \phi_\theta) = (\frac{\pi}{4}, -\frac{3\pi}{4})$.

Consider the case where $A_y = 1$, $A_\theta = \frac{\pi}{4}$, $\phi_y = -\frac{\pi}{2}$, $\phi_\theta = 0$ and consider various aspect ratios $\gamma = 1.01, 4, 8, 1000$, as shown in Figure 2. Note that as we vary the aspect ratio, the total area of the elliptic body is maintained constant, which is guaranteed by the way we non-dimensionlize length using $\sqrt{ab}$. As expected, the net locomotion is almost zero when the elliptic body is close to a circular shape ($\gamma = 1.01$) and it reaches a maximum as the elliptic body approaches a flat plate ($\gamma = 1000$).

In Figure 3, γ is set to 4 and A_y is varied. One can see that the net locomotion d depends linearly on A_y, which is also evident from (6). In Figure 4, different cases of A_θ are shown. Here, the net locomotion depends nonlinearly on A_θ. Interestingly, the trajectories

that correspond to $A_\theta = \pi/4$ and $A_\theta = \pi/8$ almost coincide, whereas for $A_\theta = 3\pi/4$ the locomotion is in the negative x direction.

Motions for various phases ϕ_y and ϕ_θ are shown in Figures 5. Notice the shape and orientation of the closed path in the (y, θ) parameter space depend on the difference in phase $\phi_y - \phi_\theta$. This can be readily verified by eliminating t from (1) and expressing the closed path in the (y, θ) plane as

$$\left(\frac{y}{A_y}\right)^2 - 2\frac{y}{A_y}\frac{\theta}{A_\theta}\cos(\phi_y - \phi_\theta) + \left(\frac{\theta}{A_\theta}\right)^2 = \sin^2(\phi_y - \phi_\theta). \tag{15}$$

In other words, as $\phi_y - \phi_\theta$ varies, the closed path in the (y, θ) plane is elliptic, except for $\phi_y - \phi_\theta = n\pi$ $(n = 0, \pm 1, \pm 2, \ldots)$ in which case it is a segment of the straight line given by $\theta = (-1)^n (A_\theta/A_y) y$. Further, notice that the the dependence of resulting locomotion $x(t)$ in (6) on the flapping motion $x(y(t), \theta(t))$ possesses the following symmetries

$$x(-y, -\theta) = x(y, \theta), \quad x(-y, \theta) = -x(y, \theta), \quad x(y, \theta) = -x(y, \theta). \tag{16}$$

whereas the flapping motion in (1) has the following symmetries

$$\begin{aligned} y(t; \phi_y + \pi) &= -y(t; \phi_y), \qquad y(-t; \phi_y) = -y(t; -\phi_y), \\ \theta(t; \phi_\theta + \pi) &= -\theta(t; \phi_\theta), \qquad \theta(-t; \phi_\theta) = -\theta(t; -\phi_\theta). \end{aligned} \tag{17}$$

Based on these symmetries, one can immediately conclude that, when all other parameters are held fix, motions that correspond to (ϕ_y, ϕ_θ) and $(-\phi_y, -\phi_\theta)$ are mirror images of each other: their distances and energies are the same, which can be seen from (16). Also, for combinations (ϕ_y, ϕ_θ) with $\phi_y - \phi_\theta = 2n\pi + \text{constant}$, they result in the same path in the (y, θ) space. When tracing the same path in the (y, θ) plane (but starting at different initial points), the resulting trajectories in the (x, y) plane are very similar (with different initial positions). One might be tempted to jump to the conclusion that tracing a straight line in the (y, θ) plane corresponds to zero net locomotion in the (x, y) plane. This is true for $\phi_y = \phi_\theta = 0$ and $\phi_y = \phi_\theta = -\pi/2$, but it is not true in general as evident from the example of $\phi_y = \pi/4, \phi_\theta = -3\pi/4$ in Figure 5(h). This is unlike the well known result in geometric mechanics that zero enclosed area in shape space results in zero net locomotion, see [7]. Indeed, the locomotion here is not a result of a geometric phase but rather of a dynamic phase.

While the numerical results in Figures 2 to 5 provide an understanding of the average distance d travelled over one period T of flapping, the average work $\bar{E}$ is not reflected and remains to be computed. More specifically, we are interested in the cost of locomotion $e = \bar{E}/d$, which we compute numerically. Ideally, one would like to find optimal parameter values that minimize e (maximize efficiency η) and/or maximize d (see, for example [3, 12]). It is computationally expensive to do an exhaustive search to minimize e over the five dimensional parameter space. Instead, similar to the locomotion study, we focus on varying one parameter at a time. In Figure 6, we set $\phi_y = -\frac{\pi}{2}, \phi_\theta = 0$ while γ, A_y and A_θ are varied in (a), (b) and (c), respectively. Solid lines are nonlinear numerical solutions, and dashed lines are obtained by substituting the parameters into (13). Figure 6(a) shows that, for $A_y = 1, A_\theta = \pi/4$, there exist a optimal value of $\gamma \approx 2.9$, whereas the small amplitude approximation in (13)

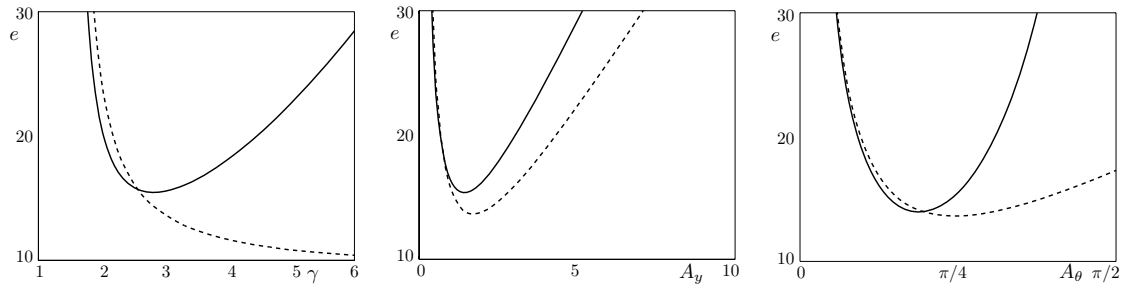

(a) e vs. γ (b) e vs. A_y (c) e vs. A_θ

Figure 6: Cost of locomotion e as a function of: (a) aspect ratio γ, (b) heaving amplitude A_y, (c) pitching amplitude A_θ. The base parameter values are set to $\phi_y = -\pi/2, \phi_\theta = 0$, $\gamma = 4$, $A_\theta = \pi/4$, $A_y = 1$. Solid lines are nonlinear numerical solutions, while dashed lines are based on small amplitude approximation given in (13).

(shown in dashed line in the figure) predicts that e is a decreasing function of γ. Similarly, Figures 6(b) and (c) show optimal values of $A_y \approx 1.3$ and $A_\theta \approx \frac{3\pi}{16}$. One can see that the small amplitude results qualitatively follows the nonlinear behavior of e for the parameter A_y. This is not surprising given that the work E depends quadratically on A_y, the displacement d depends linearly on A_y and that the small amplitude approximation in (13) preserves the form of dependence on this parameter. However, in the case of varying A_θ, the small amplitude results can approximate the nonlinear efficiency up to $A_\theta \approx \frac{3\pi}{16}$, but start to deviate from the nonlinear results thereafter.

In Figure 7 to 9, we examine the dependence of e on the phases by discretizing (ϕ_y, ϕ_θ) on a 201×201 mesh in the range of $[-\pi\,,\,\pi] \times [-\pi\,,\,\pi]$ (which is representative of the entire plane due to periodicity). Contours of e are depicted for various γ, A_y and A_θ as a function of (ϕ_y, ϕ_θ). Indeed, it is sufficient to only show the dependence of e on one quarter of the shown region, say, $[0\,,\,\pi] \times [0\,,\,\pi]$, because of the reflection symmetry about the origin $e(\phi_y, \phi_\theta) = e(-\phi_y, -\phi_\theta)$ and the periodicity of π in efficiency $e(\phi_y + \pi, \phi_\theta + \pi) = e(\phi_y, \phi_\theta)$, both of which can be easily obtained from (16-17).

Note that the parameters that minimize e, thus maximize efficiency η, are approximately $3 \le \gamma \le 4, A_y \approx 1.3$, $A_\theta \approx 3\pi/16$ and $(\phi_y, \phi_\theta) \approx ((m + \frac{1}{2})\pi, n\pi)$, where $m, n = 0, \pm 1, \pm 2, \ldots$ One example of the optimal phases is $\phi_y = \frac{\pi}{2}, \phi_\theta = 0$, whose corresponding locomotion and snapshots of dynamics are shown in Figure 2. For this optimal motion, the pitching angle is zero when the heaving motion is maximum (90° out of phase), which qualitatively agrees the results in [12]. The optimal aspect ratio $3 \le \gamma \le 4$ agrees with the optimal shape aspect ratio obtained in the optimization study in [3], and is representative of the aspect ratio of various Carangiform swimmers such as bass ($\gamma = 3.8$) in [13], tuna ($\gamma = 3.5$) in [14] and saithe ($\gamma = 4.1$) in [15]. The optimal heave to cord ratio $A_y/a \approx 0.75$ (where $a = \sqrt{\gamma} \approx \sqrt{3}$) and maximum angle $A_\theta \approx 3\pi/16 = 16.875°$ both agree with the optimal motions for the rigid flapping body ($0.75 \le A_y/a \le 1, A_\theta \approx 16°$) given in [16].

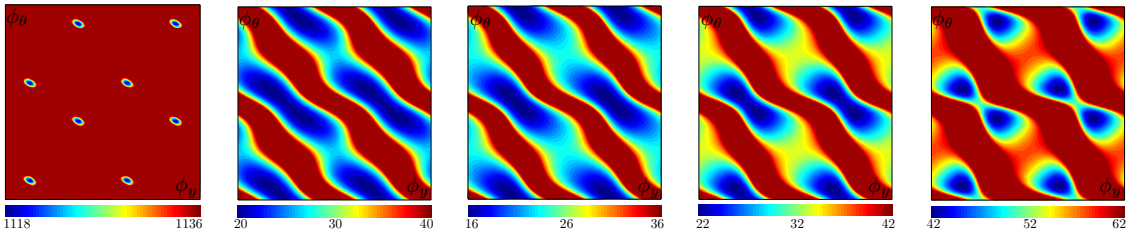

(a) $\gamma = 1.01$ (b) $\gamma = 2$ (c) $\gamma = 4$ (d) $\gamma = 8$ (e) $\gamma = 16$

Figure 7: Contour plots of cost of locomotion e for the cases $A_y = 1, A_\theta = \pi/4$ and various aspect ratio γ. Each plot is evaluated on a 201×201 mesh in $[-\pi\,,\,\pi] \times [-\pi\,,\,\pi]$ in (ϕ_y, ϕ_θ) plane. Lower value of e corresponds to higher efficiency.

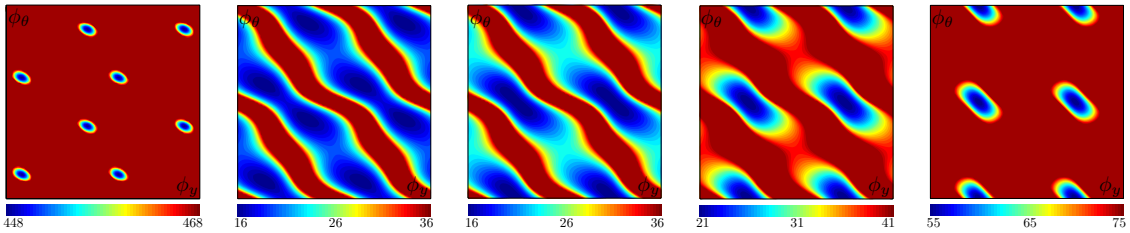

(a) $A_y = 0.01$ (b) $A_y = 0.5$ (c) $A_y = 1$ (d) $A_y = 2$ (e) $A_y = 6$

Figure 8: Contour plots of cost of locomotion e for the cases $A_\theta = \pi/4$, $\gamma = 4$ and various heaving amplitude A_y. Each plot is evaluated on a 201×201 mesh in $[-\pi\,,\,\pi] \times [-\pi\,,\,\pi]$ in (ϕ_y, ϕ_θ) plane. Lower value of e corresponds to higher efficiency.

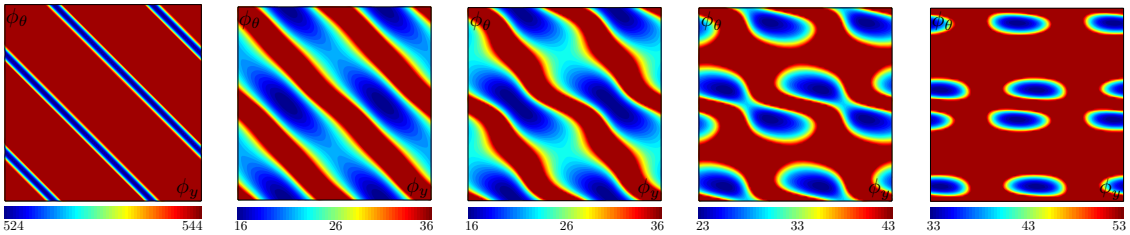

(a) $A_\theta = 0.01$ (b) $A_\theta = \pi/8$ (c) $A_\theta = \pi/4$ (d) $A_\theta = 3\pi/8$ (e) $A_\theta = \pi/2$

Figure 9: Contour plots of cost of locomotion e for the cases $A_y = 1$, $\gamma = 4$ and various pitching amplitude A_θ. Each plot is evaluated on a 201×201 mesh in $[-\pi\,,\,\pi] \times [-\pi\,,\,\pi]$ in (ϕ_y, ϕ_θ) plane. Lower value of e corresponds to higher efficiency.

5 Stability of Periodic Locomotion

We study stability of periodic motion subject to arbitrary perturbations in the surrounding fluid. We begin by introducing $\mathbf{q} = [\dot{x}, \dot{y}, \theta, \dot{\theta}]^T$, and rewriting (2) and (3) as follows

$$\mathbb{M}(\theta)\dot{\mathbf{q}} = \mathbf{f}(\mathbf{q}) + \mathbf{F}^{\text{flap}}, \tag{18}$$

where detailed expressions for $\mathbb{M}$, $\mathbf{f}$ and $\mathbf{F}^{\text{flap}}$ are listed in Appendix B. In Sections 2–4, we prescribed the flapping motion $y(t)$ and $\theta(t)$ according to (1) and used (6) to solve for $x(t)$ and (3) to solve for F^{flap} and τ^{flap} necessary to produce the flapping motion. The resulting

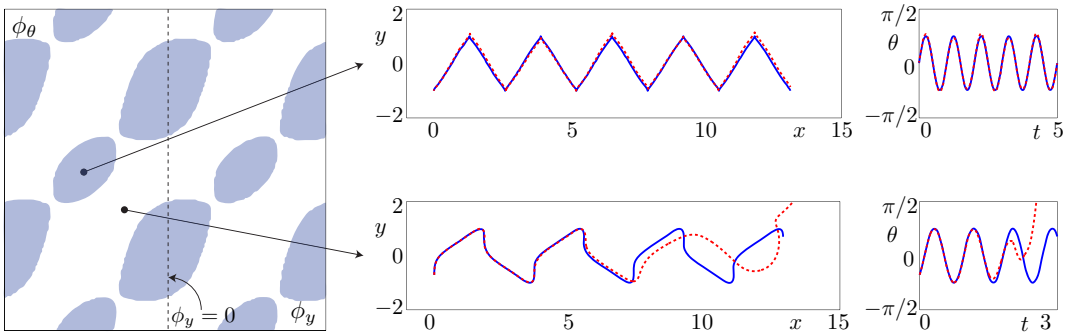

Figure 10: Left: stability of the case $A_y = 1$, $A_\theta = \pi/4$ and $\gamma = 4$, with phases (ϕ_y, ϕ_θ) varied on a 201×201 mesh in $[-\pi\,,\,\pi] \times [-\pi\,,\,\pi]$. Stable cases correspond to shaded areas, unstable cases are white areas. Middle and right: (top) $(\phi_y, \phi_\theta) = (-\pi/2, 0)$ is stable. Solid lines correspond to unperturbed periodic solutions, dashed lines correspond to perturbed solutions; (bottom) $(\phi_y, \phi_\theta) = (-\pi/4, -\pi/4)$ is unstable.

motion $x(t)$, $y(t)$, and $\theta(t)$ as well as the forcing F^{flap} and τ^{flap} are periodic with period T. We let $\mathbf{q}_p$ denote the $\mathbf{q}$ corresponding to such periodic motion. We study the stability of $\mathbf{q}_p$ by introducing a small perturbation $\delta\mathbf{q}$ such that $\mathbf{q} = \mathbf{q}_p + \delta\mathbf{q}$ while keeping F^{flap} and τ^{flap} the same as that producing the periodic solution. In other words, we account for arbitrary perturbations in the fluid environment while keeping the same flapping forces to check if such perturbations destabilize the periodic trajectory.

Linearizing equation (18) about the periodic trajectory $\mathbf{q}_p(t)$, one gets

$$\delta\dot{\mathbf{q}} = \mathbb{J}(t)\delta\mathbf{q}, \tag{19}$$

where the Jacobian $\mathbb{J}(t)$ is a 4×4 matrix, and it has period T, that is, $\mathbb{J}(0) = \mathbb{J}(T)$,

$$\mathbb{J}(t) = \left.\frac{\partial \mathbf{g}}{\partial \mathbf{q}}\right|_{(\mathbf{q}_p, \mathbf{F}^{\text{flap}})} \quad \text{where} \quad \mathbf{g} = \mathbb{M}^{-1}(\mathbf{f} + \mathbf{F}^{\text{flap}}). \tag{20}$$

See Appendix B for details. Let $\Phi(t)$ denote the *fundamental solution matrix* of (19). The eigenvalues λ_i of the time-independent matrix,

$$B = \Phi(0)^{-1}\Phi(T). \tag{21}$$

are referred to as the *characteristic multipliers*. Their locations in the complex plane indicate the stability of the periodic solution $\mathbf{q}_p$: if any of the λ_i's lies *outside* the unit circle, then $\mathbf{q}_p$ is unstable; if all λ_i are *on* the unit circle, then $\mathbf{q}_p$ is regarded to as marginally stable. For a non dissipative system like our model, these two are the only possible scenarios, namely, unstable or marginally stable (simply referred to as "stable" hereafter). One eigenvalue λ_1 is always 1, reflecting the fact that $\mathbf{q}_p$ is periodic. The other eigenvalues may be complex. If, say, λ_2 and λ_3 are complex, they come in conjugate, i.e. $\lambda_2 = \overline{\lambda_3}$. the fourth eigenvalue λ_4 must be real.

We determine stability by computing the characteristic multipliers of the 4-dimensional system described in (19). For the case $A_y = 1, A_\theta = \frac{\pi}{4}, \gamma = 4$, the stability results are plotted in Figure 10 as a function of the phases (ϕ_y, ϕ_θ), again evaluated on a 201×201 mesh in $[-\pi\,,\,\pi] \times [-\pi\,,\,\pi]$. The stable regions are shaded areas, and the unstable regions

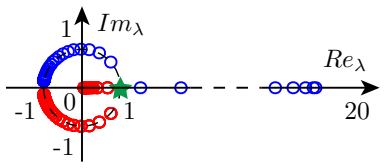

(a) Real vs. Imaginary parts of λ_i

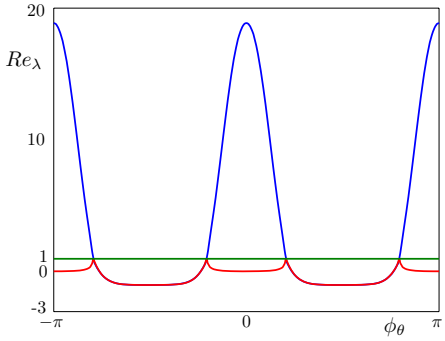

(b) Real parts of λ_i vs. ϕ_θ

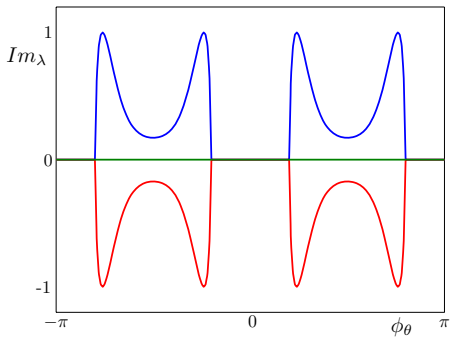

(c) Imaginary parts of λ_i vs. ϕ_θ

Figure 11: (Color online) Characteristic multipliers of the cases $A_y = 1, A_\theta = \pi/4, \gamma = 4, \phi_y = 0$, and ϕ_θ varied from $-\pi$ to π: (a) Real and Imaginary parts in complex plane. Two characteristic multipliers always locate at $(1, 0)$ are represented by ★. The two complex conjugates are represented by ◯. (b) Real and (c) Imaginary parts of characteristic multipliers. Motion becomes unstable when the two complex conjugates collide at $(1, 0)$ and split on real axis.

are white areas. Notice the reflection symmetry about $(0, 0)$ and periodicity of π in both ϕ_y and ϕ_θ that we observed in the efficiency analysis is again seen in the stability plot. Two examples with different stability characteristics are shown. The solid lines are unperturbed periodic solutions $\mathbf{q}_p$, and dashed lines are solutions with random initial perturbations with magnitude $|\delta\mathbf{q}(t = 0)| \sim O(10^{-3})$. Clearly, the trajectory corresponding to parameters in the stable region remain close to the periodic trajectory for the integration time whereas that corresponding to parameters in the unstable region does not.

In Figure 11, we examine the behavior of the real and imaginary parts of the characteristic multipliers as a function of ϕ_θ for $A_y = 1, A_\theta = \pi/4, \gamma = 4$ and $\phi_y = 0$. In other words, we explore the behavior of λ_i's as we cross the (ϕ_y, ϕ_θ) space along the dashed line corresponding to $\phi_y = 0$ in the left plot of Figure 10. One can see that two characteristic multipliers are always located at $(1, 0)$ (represented by ★). The other two are represented by ◯. The dynamics changes from stable to unstable when the two conjugates collide at $(1, 0)$ and split onto real axis. For the considered parameters, when ϕ_θ varies from $-\pi$ to π, stability changes from unstable to stable and stable to unstable four times in total.

We now show how stability changes with γ, A_y and A_θ by varying them one at a time while keeping the others constant. Figure 12 shows stability regions for $A_y = 1, A_\theta = \frac{\pi}{4}$, and various aspect ratio γ. For bodies closer to circular shape ($\gamma = 1.01$), the motion is stable for all (ϕ_y, ϕ_θ) (but not useful since net displacement is almost zero). When $\gamma > 1.43$, unstable regions start to appear as strips. As γ increases, unstable regions grow while stable regions shrink. The total area of stable regions becomes minimum when $\gamma \approx 2$, and the

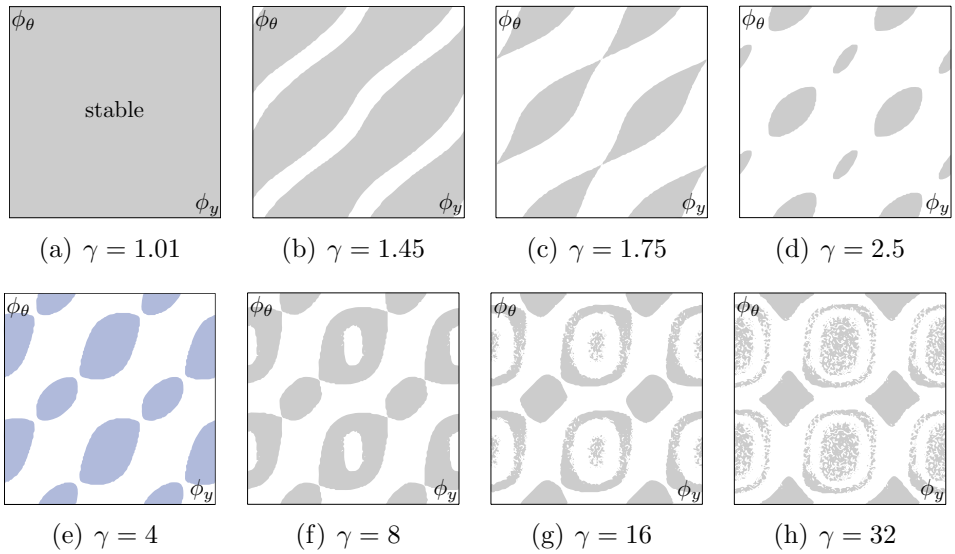

(a) $\gamma = 1.01$ (b) $\gamma = 1.45$ (c) $\gamma = 1.75$ (d) $\gamma = 2.5$

(e) $\gamma = 4$ (f) $\gamma = 8$ (g) $\gamma = 16$ (h) $\gamma = 32$

Figure 12: Stability regions for the cases $A_y = 1, A_\theta = \pi/4$ and various aspect ratio γ. Each plot is evaluated on a 201×201 mesh in $[-\pi\,,\,\pi] \times [-\pi\,,\,\pi]$ in (ϕ_y, ϕ_θ) plane. Shaded areas correspond to stable cases, white areas correspond to unstable cases.

stable areas remain around $(\phi_y, \phi_\theta) = ((m + 1/2)\pi, n\pi)$. Interestingly, as γ continues to increase, new stable regions start to emerge and grow from the previous unstable areas around $(\phi_y, \phi_\theta) = (n\pi, (m+1/2)\pi)$. Then, at these spots, unstable regions emerge and grow from the newly formed stable regions, and so on and so forth. The boundaries between stable and unstable regions around $(n\pi, (m+1/2)\pi)$ become blurry as γ becomes larger, and $((m+1/2)\pi, n\pi)$ remain stable. Overall, the total area of stable regions recovers. This trend is reminiscent of the phenomenon observed in Spagnolie et al. [10], in which the authors noticed the motion of an elliptic body subject to prescribed heaving motion and passive pitching motion goes through states from "coherence to incoherence, and back again" as the aspect ratio changes. Note that the latter studies are in viscous fluid whereas the analysis here is for an inviscid fluid model. Still, this simplified model is able to capture, at least, qualitatively, the behavior observed in [10].

Figure 13 shows stability regions for $A_\theta = \pi/4, \gamma = 4$ and various A_y. For small A_y such as 0.01, the body is mostly rotating, and the motion is stable for all (ϕ_y, ϕ_θ) but with no net locomotion. As A_y increases, unstable regions start to form around $(n\pi, (m+1/2)\pi)$, as can be seen in Figure 13(c). As A_y continues to increase, unstable regions grow while stable regions shrink. Then, layers of stable/unstable regions start to form around $(n\pi, (m+1/2)\pi)$. Unlike previous trend when γ is varied, areas around $((m+1/2)\pi, n\pi)$ do not remain stable. Instead, the stable/unstable layers also form there. Overall, the total area of stable regions decreases as A_y becomes larger. The area and shape of stable regions depend nonlinearly on A_y, which is an interesting result since the trajectory of the mass center depends *linearly* on A_y.

Finally, we vary A_θ while keeping $A_y = 1$ and $\gamma = 4$ in Figure 14. When A_θ is small, the whole plane in (ϕ_y, ϕ_θ) is stable but again does not result in net locomotion. As A_θ increases, unstable regions start to emerge and grow, while stable regions shrink and remain

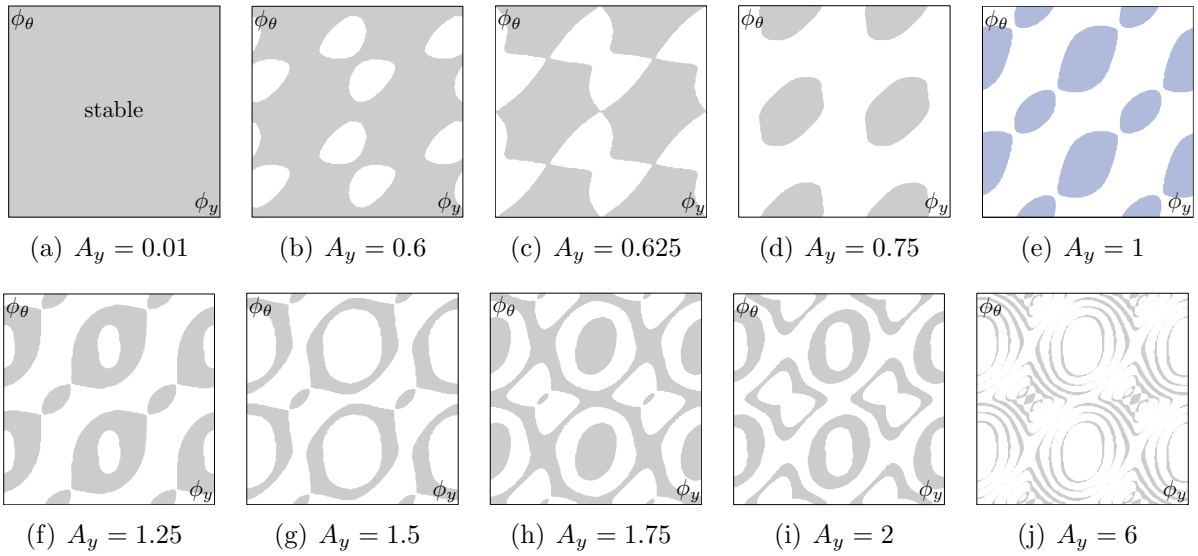

(a) $A_y = 0.01$ (b) $A_y = 0.6$ (c) $A_y = 0.625$ (d) $A_y = 0.75$ (e) $A_y = 1$

(f) $A_y = 1.25$ (g) $A_y = 1.5$ (h) $A_y = 1.75$ (i) $A_y = 2$ (j) $A_y = 6$

Figure 13: Stability regions for the cases $A_\theta = \pi/4$, $\gamma = 4$ and various heaving amplitude A_y. Each plot is evaluated on a 201×201 mesh in $[-\pi\,,\,\pi] \times [-\pi\,,\,\pi]$ in (ϕ_y, ϕ_θ) plane. Shaded areas correspond to stable cases, white areas correspond to unstable cases.

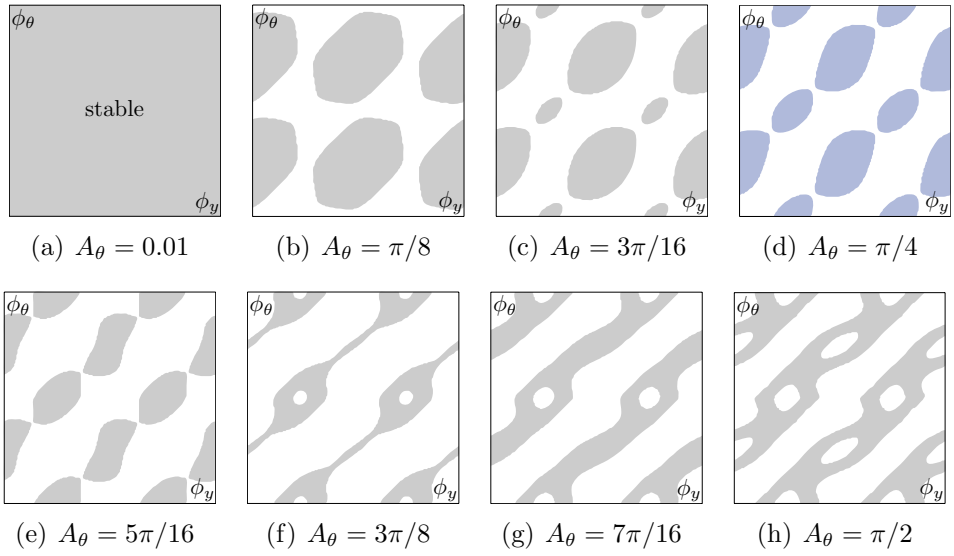

(a) $A_\theta = 0.01$ (b) $A_\theta = \pi/8$ (c) $A_\theta = 3\pi/16$ (d) $A_\theta = \pi/4$

(e) $A_\theta = 5\pi/16$ (f) $A_\theta = 3\pi/8$ (g) $A_\theta = 7\pi/16$ (h) $A_\theta = \pi/2$

Figure 14: Stability regions for the cases $A_y = 1$, $\gamma = 4$ and various pitching amplitude A_θ. Each plot is evaluated on a 201×201 mesh in $[-\pi\,,\,\pi] \times [-\pi\,,\,\pi]$ in (ϕ_y, ϕ_θ) plane. Shaded areas correspond to stable cases, white areas correspond to unstable cases.

around $(n\pi, (m + 1/2)\pi)$. However, as A_θ continue to increase, the stable regions gradually become strip-like shaped roughly along $\phi_\theta - \phi_y = (m + \frac{1}{2})\pi$. And unstable regions start to emerge within the stable strips.

This trend of switching from stability to instability and back to stability that is observed when varying each of the parameters is extremely interesting. It suggests that such swimmers can change their stability character by changing their flapping motion, and thus can easily

switch from stable periodic swimming to an unstable motion (more maneuverable) when they feel the need to, such as when evading a predator. Based on this, one can conjecture that when it comes to live organisms, maneuverability and stability need not be thought of as disjoint properties, rather the organism may manipulate its motion in favor of one or the other depending on the task at hand. Experimental results that show that live organisms change their stability properties at will are yet to be established.

6 Discussion and Conclusion

We studied the locomotion, efficiency and stability of periodic swimming of fish using a simple planar model of elliptic swimmer undergoing prescribed sinusoidal heaving and pitching motion in potential flow. We obtained expressions for the locomotion velocity for both small and finite flapping amplitudes, and showed how trajectories depend on key parameters, namely, aspect ratio γ, amplitudes A_y and A_θ and phases ϕ_y and ϕ_θ. Efficiency is defined as the inverse of cost of locomotion e. We studied the dependence of e on the parameters for both small and finite amplitude flappings. We observed that the efficiency maximizing parameters are approximately $3 \leq \gamma \leq 4, A_y \approx 1.3, A_\theta \approx \frac{3\pi}{16}, \phi_y \approx (m + \frac{1}{2})\pi$ and $\phi_\theta \approx n\pi$, where $n, m = 0, \pm 1, \pm 2, \ldots$, whose values are in excellent agreement with results based on experimental and computational motions of flapping fish, see [3, 16, 12] and references therein.

We then studied the stability of periodic locomotion using Floquet theory. To our best knowledge, besides the work of Weihs which uses approximate arguments, this is the first work that rigorously studies the stability of periodic locomotion albeit in a simplified model. We focused on evaluating stability on the whole (ϕ_y, ϕ_θ) parameter space, and examined the effect of varying γ, A_y and A_θ on the resulting stability. We observed that stable and unstable regions in the (ϕ_y, ϕ_θ) plane evolved as these parameters change. Particularly noteworthy is the back and forth switching between stability and instability around the spots $((m+\frac{1}{2})\pi, n\pi)$ and $(n\pi, (m + \frac{1}{2})\pi)$. This switching is reminiscent to the observation in [10] that the motion of a heaving and pitching foil switches from coherence to incoherence and back to coherence when varying the aspect ratio of foil. In our study, we found a similar behavior when varying not only the aspect ratio but also the flapping parameters. This indicates that the swimmer can change its stability character by changing its flapping motion, and thus can easily switch from stable periodic swimming to an unstable, yet more maneuverable, state. Based on this, one could conjecture that, when it comes to live organisms, maneuverability and stability need not be thought of as disjoint properties, rather the organism may manipulate its motion in favor of one or the other depending on the task at hand. Clearly, this statement is speculative until verified by experimental evidence. To date, little is known experimentally on the stability of underwater periodic motions, let alone the stability of biological swimmers.

Future extensions of the current work may include studying the effects of body deformation and body elasticity on the observed stability of periodic swimming. In a planer potential flow, a model of articulated body that can undergo shape change, and with torsional springs attached to the joint to mimic the effect of fish muscle elasticity can be implemented (similar to the ones studied in [7, 8, 9]). One may also be interested to study the effect of different frequencies of heaving and pitching motions (assumed to be equal in this work), and further-

more the effect of frequency in shape change (see [17]) on the stability result. The current model makes the assumption of zero vorticity in the potential flow, which simplifies the analysis and focuses on the added mass effect from the surrounding fluid. A natural extension is to include vortex shedding in the system, and use vortex sheet method [18] or Brown-Michael model [19] to study the effect of coupled body-vortex system on the aforementioned stability results.

Appendix A: Hydrodynamic Forces and Moments

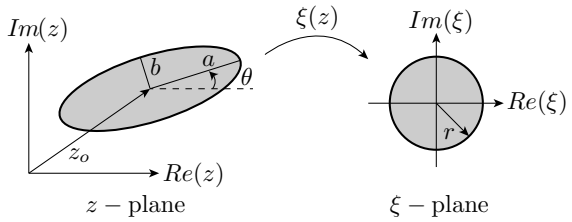

Figure 15: Exterior region of the ellipse of semi-axes a and b in the complex z-plane is mapped to the exterior region of a circle with radius $r = (a+b)/2$ in the ξ-plane. The mapping is given by (22).

In potential flow, the fluid forces F_x, F_y and moment τ can be obtained from the *added-mass theory* [20] or from the *extended Blasius theorem* [20, 21, 22]. In this appendix, we present both derivations and show their equivalence.

The exterior region of the ellipse in the complex z-plane ($z = x + iy$) is mapped to the exterior region of a circle with radius $r = (a+b)/2$ in the ξ-plane, see Figure 15. The mapping is given by

$$z - z_o = \left(\xi + \frac{c^2}{\xi}\right) e^{i\theta}, \quad \text{or equivalently,} \quad \xi = \frac{(z-z_o)e^{-i\theta}}{2} + \frac{\sqrt{(z-z_o)^2 e^{-2i\theta} - 4c^2}}{2}, \tag{22}$$

where $c = \sqrt{a^2 - b^2}/2$. The complex potential of the fluid in ξ-plane is given by [22],

$$W(\xi) = \frac{\overline{U} r^2 - U c^2}{\xi} - \frac{i\dot{\theta} r^2 c^2}{\xi^2}, \tag{23}$$

where $U = -\dot{\bar{z}}_c e^{i\theta}$ is the velocity of the mass center mapped into the ξ-plane. Therefore, the forces and moment exerted by the surrounding fluid on a moving body are given by the *extended Blasius theorem* [21]. In z-plane,

$$F_x + iF_y = \overline{\frac{i\rho}{2} \oint_{\partial\mathcal{B}} \left(\frac{\mathrm{d}W}{\mathrm{d}z}\right)^2 \mathrm{d}z} + i\rho \frac{\mathrm{d}}{\mathrm{d}t} \left[\oint_{\partial\mathcal{B}} (z - z_o) \frac{\mathrm{d}W}{\mathrm{d}z} \mathrm{d}z\right] + \rho A_{\mathcal{B}} \ddot{z}_o,$$

$$\tau = \frac{\rho}{2} \mathrm{Re}\left[2\dot{\bar{z}}_o \oint_{\partial\mathcal{B}} (z - z_o) \frac{\mathrm{d}W}{\mathrm{d}z} \mathrm{d}z - \oint_{\partial\mathcal{B}} (z - z_o) \left(\frac{\mathrm{d}W}{\mathrm{d}z}\right)^2 \mathrm{d}z + \frac{\mathrm{d}}{\mathrm{d}t} \left(\oint_{\partial\mathcal{B}} |z - z_o|^2 \frac{\mathrm{d}W}{\mathrm{d}z} \mathrm{d}z\right)\right], \tag{24}$$

where $A_{\mathcal{B}} = \pi ab$ is the area of the ellipse, $\partial\mathcal{B}$ is the boundary of the body, and the reader is reminded that the densities of the body and fluid are both ρ. Notice that the last term in τ needs to be treated separately. All other integrals are analytic and, using residual theory, can be taken around an infinitely large circle instead of the boundary of the body, which greatly simplifies the calculations. For the last term in moment, since $|z - z_o|^2$ is not analytic, one cannot use this technique. Instead, it needs to be integrated on the boundary. Substituting (22) and (23) into (24), one obtains the hydrodynamic forces and moment given by

$$\begin{aligned} F_x &= \pi\rho\left(-\frac{r^4+c^4}{r^2} + 2c^2\cos 2\theta\right)\ddot{x} + 2\pi\rho c^2\ddot{y}\sin 2\theta - 4\pi\rho c^2\dot{\theta}(\dot{x}\sin 2\theta - \dot{y}\cos 2\theta), \\ F_y &= \pi\rho\left(-\frac{r^4+c^4}{r^2} - 2c^2\cos 2\theta\right)\ddot{y} + 2\pi\rho c^2\ddot{x}\sin 2\theta + 4\pi\rho c^2\dot{\theta}(\dot{x}\cos 2\theta + \dot{y}\sin 2\theta), \\ \tau &= 2\pi\rho c^2\left(\dot{x}^2\sin 2\theta - \dot{y}^2\sin 2\theta - 2\dot{x}\dot{y}\cos 2\theta - c^2\ddot{\theta}\right). \end{aligned} \tag{25}$$

Since

$$2\pi\rho c^2 = \frac{m_2 - m_1}{2}, \quad \pi\rho\frac{r^4+c^4}{r^2} = \frac{m_1+m_2}{2}, \quad 2\pi\rho c^4 = J,$$

the hydrodynamical forcing terms are equivalent with the expressions given in (4), which is repeated here for completeness,

$$\begin{aligned} F_x &= \frac{1}{2}\left[-(m_1+m_2) + (m_2-m_1)\cos 2\theta\right]\ddot{x} + \frac{1}{2}(m_2-m_1)\ddot{y}\sin 2\theta - (m_2-m_1)(\dot{x}\sin 2\theta - \dot{y}\cos 2\theta)\dot{\theta}, \\ F_y &= \frac{1}{2}\left[-(m_1+m_2) - (m_2-m_1)\cos 2\theta\right]\ddot{y} + \frac{1}{2}(m_2-m_1)\ddot{x}\sin 2\theta + (m_2-m_1)(\dot{x}\cos 2\theta + \dot{y}\sin 2\theta)\dot{\theta}, \\ \tau &= -J\ddot{\theta} + \frac{1}{2}(m_2-m_1)\left(\dot{x}^2\sin 2\theta - \dot{y}^2\sin 2\theta - 2\dot{x}\dot{y}\cos 2\theta\right). \end{aligned}$$

And the governing equations are again repeated here

$$m_b\ddot{x} = F_x, \quad m_b\ddot{y} = F_y + F^{\text{flap}}, \quad J_b\ddot{\theta} = \tau + \tau^{\text{flap}}. \tag{26}$$

When expressed in a body-fixed frame, the hydrodynamic forces and moment take a simpler form in terms of the *added mass coefficients* m_1, m_2 and J. Roughly speaking, as a body moves through potential flow, the body-fluid system behaves as an augmented body with modified mass and inertia that account for the added mass and added inertia due to the presence of the fluid. The added mass and inertia depend only on the geometry of the body and direction of motion. The Kirchhoff's equations of motion in terms of the body-fixed frame variables are given by

$$\begin{aligned} (m_b+m_1)\dot{V}_1 &= -(m_b+m_2)V_2\Omega + F_1, \\ (m_b+m_2)\dot{V}_2 &= (m_b+m_1)V_1\Omega + F_2, \\ (J_b+J)\dot{\Omega} &= (m_1-m_2)V_1V_2 + \tau^{\text{flap}}, \end{aligned} \tag{27}$$

where the body frame velocities and forces are given by

$$\begin{pmatrix} V_1 \\ V_2 \end{pmatrix} = \begin{pmatrix} \cos\theta & \sin\theta \\ -\sin\theta & \cos\theta \end{pmatrix}\begin{pmatrix} \dot{x} \\ \dot{y} \end{pmatrix}, \quad \Omega = \dot{\theta}, \quad \text{and} \quad \begin{pmatrix} F_1 \\ F_2 \end{pmatrix} = \begin{pmatrix} \cos\theta & \sin\theta \\ -\sin\theta & \cos\theta \end{pmatrix}\begin{pmatrix} F_x \\ F_y \end{pmatrix},$$

and τ is the same form in inertial frame. Transforming (27) via a rotation θ to inertial frame, one obtains the equations given in (2) and (3), and the hydrodynamical forcing terms are given by (4). It is then straightforward to verify that (26) and (27) are equivalent.

Appendix B: Floquet theory

For completeness, we repeat (18) here

$$\mathbb{M}(\theta)\dot{\mathbf{q}} = \mathbf{f}(\mathbf{q}) + \mathbf{F}^{\text{flap}},$$

where

$$\mathbb{M}(\theta) = \begin{pmatrix} \frac{r^2}{c^2} - \cos 2\theta & -\sin 2\theta & 0 & 0 \\ -\sin 2\theta & \frac{r^2}{c^2} + \cos 2\theta & 0 & 0 \\ 0 & 0 & 1 & 0 \\ 0 & 0 & 0 & \frac{r^8 - c^8 + 4r^4c^4}{4r^4c^2} \end{pmatrix}, \tag{28}$$

and

$$\mathbf{f}(\mathbf{q}) = \begin{pmatrix} -2\dot{\theta}\dot{x}\sin 2\theta + 2\dot{\theta}\dot{y}\cos 2\theta \\ 2\dot{\theta}\dot{x}\cos 2\theta + 2\dot{\theta}\dot{y}\sin 2\theta \\ \dot{\theta} \\ (\dot{x}^2 - \dot{y}^2)\sin 2\theta - 2\dot{x}\dot{y}\cos 2\theta \end{pmatrix}, \qquad \mathbf{F}^{\text{flap}} = \frac{1}{2\rho\pi c^2}\begin{pmatrix} 0 \\ F^{\text{flap}} \\ 0 \\ \tau^{\text{flap}} \end{pmatrix}. \tag{29}$$

Hence, the equations of motion can be rewritten by taking inverse of $\mathbb{M}$,

$$\dot{\mathbf{q}} = \mathbf{g} \equiv \mathbb{M}^{-1}(\mathbf{f} + \mathbf{F}^{\text{flap}}). \tag{30}$$

One can linearize above equation and obtain

$$\delta\dot{\mathbf{q}} = \mathbb{J}(t)\delta\mathbf{q}, \qquad \text{where} \qquad \mathbb{J}(t) = \left.\frac{\partial \mathbf{g}}{\partial \mathbf{q}}\right|_{(\mathbf{q}_p, \mathbf{F}^{\text{flap}})},$$

and the entries of the Jacobian $\mathbb{J}(t)$ are given by

$$\mathbb{J}(t) = \begin{pmatrix} \frac{2r^2c^2\dot{\theta}\sin 2\theta}{-r^4 + c^4} & \frac{2c^2\dot{\theta}(c^2 + r^2\cos 2\theta)}{r^4 - c^4} & \mathbb{J}_{13} & \mathbb{J}_{14} \\ \frac{2c^2\dot{\theta}(c^2 - r^2\cos 2\theta)}{-r^4 + c^4} & \frac{2r^2c^2\dot{\theta}\sin 2\theta}{r^4 - c^4} & \mathbb{J}_{23} & \mathbb{J}_{24} \\ 0 & 0 & 0 & 1 \\ \mu\alpha & -\mu\beta & \mu\left[(\dot{x}^2 - \dot{y}^2)\cos 2\theta + 2\dot{x}\dot{y}\sin 2\theta\right] & 0 \end{pmatrix}, \tag{31}$$

where

$$\alpha = \dot{x}\sin 2\theta - \dot{y}\cos 2\theta, \quad \beta = \dot{y}\sin 2\theta + \dot{x}\cos 2\theta, \quad \mu = 8r^4c^2/(r^8 - c^8 + 4r^4c^4),$$

$$\mathbb{J}_{13} = \frac{c^2}{\rho\pi(r^4 - c^4)}\left[F^{\text{flap}}\cos 2\theta - 4r^2\rho\pi\beta\dot{\theta}\right], \quad \mathbb{J}_{14} = \frac{2c^4}{r^4 - c^4}\left[-\dot{x}r^2\sin 2\theta + \dot{y}(c^2 + r^2\cos 2\theta)\right],$$

$$\mathbb{J}_{23} = \frac{c^2}{\rho\pi(r^4 - c^4)}\left[F^{\text{flap}}\sin 2\theta - 4r^2\rho\pi\alpha\dot{\theta}\right], \quad \mathbb{J}_{24} = \frac{2c^4}{r^4 - c^4}\left[\dot{x}(c^2 - r^2\cos 2\theta) - \dot{y}r^2\sin 2\theta\right].$$

The linear equation has fundamental solution matrix $\Phi(t)$, and any solution of (19) can be expressed as a linear combination of the four columns in $\Phi(t)$. Therefore, $\Phi(T)$ can be calculated numerically by integrating (19) with initial condition $\Phi(0)$ (it is convenient then to set $\Phi(0) = I_{4\times 4}$), thus $B = \Phi(0)^{-1}\Phi(T)$ can be solved numerically. Since $\dot{x}, F^{\text{flap}}$ and τ^{flap} can be solved to machine accuracy, and analytical expression for $\mathbb{J}$ is available, B, and subsequently the characteristic multipliers, can be numerically solved to machine accuracy.

Acknowledgements

The authors would like to thank Dr. Andrew A. Tchieu and Dr. Paul K. Newton for the enlightening discussions. The work of EK is partially supported by the National Science Foundation through the CAREER award CMMI 06-44925 and the grant CCF 08-11480.

References

[1] Lighthill MJ (1970) Aquatic animal propulsion of high hydromechanical efficiency. *J. Fluid Mech.*, 44(**2**):265–301.

[2] Wu TY (2011) Fish swimming and bird/insect flight. *Annu. Rev. Fluid Mech.*, 43(**1**):25-58.

[3] Eloy C (2013) On the best design for undulatory swimming. *J. Fluid Mech.*, **717**:48–89.

[4] Weihs D (2002) Stability versus maneuverability in aquatic locomotion. *Integ. and Comp. Biol.*, 42(**1**):127–134.

[5] Weihs D (1993) Stability of aquatic animal locomotion. *Cont. Math.*, **141**:443–461.

[6] Jordan DW, Smith P (2007) *Nonlinear ordinary differential equations: an introduction to dynamical systems. (4th ed.)* Oxford Univ. Press, New York.

[7] Kanso E, Marsden JE, Rowley CW, Melli-Huber JB (2005) Locomotion of articulated bodies in a perfect fluid. *J. Nonlinear Sci.*, **15**:255-289.

[8] Jing F (2011) *Part I-Viscous evolution of point vortex equilibria, Part II-Effects of body elasticity on stability of fish motion.* PhD thesis, University of Southern California, Los Angeles.

[9] Jing F, Kanso E (2012) Effects of body elasticity on stability of underwater locomotion. *J. Fluid Mech.*, **690**:461–473.

[10] Spagnolie SE, Moret L, Shelley MJ, Zhang J (2010) Surprising behaviors in flapping locomotion with passive pitching. *Phys. Fluids*, **22**:041903.

[11] Newman JN (1977) *Marine hydrodynamics.* The MIT press, Cambridge, MA.

[12] Kern S, Koumoutsakos P (2006) Simulations of optimized anguilliform swimming. *J Exp. Biol.*, **209**:4841–4857.

[13] Jayne BC, Lauder GV (1995) Red muscle motor patterns during steady swimming in largemouth bass: Effects of speed and correlations with axial kinematics. *J. Exp. Biol.*, **198**:1575–1587.

[14] Donley JM, Dickson KA (2000) Swimming kinematics of juvenile kawakawa tuna (Euthynnus affinis) and chub mackerel (Scomber japonicus). *J. Exp. Biol.* **203**:3103–3116.

[15] Videler JJ, Hess F (1984) Fast continuous swimming of two pelagic predators, saithe (Pollachius virens) and mackerel (Scomber scombrus): A kinematic analysis. *J. Exp. Biol.* **109**:209–228.

[16] Triantafyllou MS, Hover FS, Techet AH, Yue DKP (2005) Review of hydrodynamic scaling laws in aquatic locomotion and fishlike swimming. *Appl. Mech. Rev.* 58(**4**):226–237.

[17] Jing F, Alben S (2013) Optimization of two- and three-link snakelike locomotion. *Phys. Rev. E* **87**:022711.

[18] Krasny R (1986) A study of singularity formation in a vortex sheet by the point-vortex approximation. *J. Fluid Mech.* **167**:65–93.

[19] Brown CE, Michael WH (1954) Effect of leading edge separation on the lift of a delta wing. *J. Aero. Sci.* 21(**10**):690–694.

[20] Lamb H (1932) *Hydrodynamics (6th ed.)* Cambridge Univ. Press, Cambridge.

[21] Sedov LI (1965) *Two-dimensional problems in hydrodynamics and aerodynamics. (ed. Chu CK, Cohen H, Seckler B, Gillis J)* Interscience Publishers, New York.

[22] Milne-Thomson LM (1968) *Theoretical hydrodynamics.* Dover Publications, New York.